IJMMM
International Journal of
Minerals, Metallurgy and Materials
矿物冶金与材料学报（英文版）

Promoting the microwave absorption performance of hierarchical CF@NiO/Ni composites via phase and morphology evolution

Shipeng Wang, Ziyan Liu, Qiangchun Liu, Baojun Wang, Wei Wei, Hao Wu, Zijie Xu, Shikuo Li, Fangzhi Huang, and Hui Zhang

Cite this article as:

Shipeng Wang, Ziyan Liu, Qiangchun Liu, Baojun Wang, Wei Wei, Hao Wu, Zijie Xu, Shikuo Li, Fangzhi Huang, and Hui Zhang, Promoting the microwave absorption performance of hierarchical CF@NiO/Ni composites via phase and morphology evolution, *Int. J. Miner. Metall. Mater.*, 30(2023), No. 3, pp. 494-503. https://doi.org/10.1007/s12613-022-2524-2

International Journal of Minerals, Metallurgy and Materials
Volume 30, Number 3, March 2023, Page 494
https://doi.org/10.1007/s12613-022-2524-2

Promoting the microwave absorption performance of hierarchical CF@NiO/Ni composites via phase and morphology evolution

Shipeng Wang[1)], *Ziyan Liu*[1)], *Qiangchun Liu*[4)], *Baojun Wang*[1)], *Wei Wei*[1)], *Hao Wu*[1)], *Zijie Xu*[1)], *Shikuo Li*[1,2),✉], *Fangzhi Huang*[2,3),✉], *and Hui Zhang*[1,2),✉]

1) School of Materials Science and Engineering, Anhui University, Hefei 230601, China
2) Key Laboratory of Structure and Functional Regulation of Hybrid Materials, Ministry of Education, Anhui University, Hefei 230601, China
3) School of Chemistry and Chemical Engineering, Anhui University, Hefei 230601, China
4) School of Physics and Electronic Information, Huaibei Normal University, Huaibei 235000, China
(Received: 12 April 2022; revised: 14 June 2022; accepted: 7 July 2022)

Abstract: Lightweight and efficient carbon-based microwave absorbents are significant in addressing the increasing severity of electromagnetic pollution. In this study, hierarchical NiO/Ni nanosheets with a tuneable phase and morphology supported on a carbon fiber substrate (CF@NiO/Ni) were fabricated using a hydrothermal approach and post-annealing treatment. As the annealing temperature increases, more metallic Ni is formed, and an apparent porosity appears on the sheet surface. Benefiting from the advantages of a three-dimensional (3D) conducting network, hierarchical porous structure, reinforced dipole/interface polarization, multiple scattering, and good impedance matching, the CF@NiO/Ni-500 composite exhibits an excellent microwave absorption performance even at a filling rate of only 3wt%. Specifically, its minimal reflection loss is −43.92 dB, and the qualified bandwidth is up to 5.64 GHz. In addition, the low radar cross-section area of the CF@NiO/Ni composite coating confirms its strong ability to suppress electromagnetic wave scattering. We expect that this work could contribute to a deeper understanding of the phase and morphology evolution in enhancing microwave absorption.

Keywords: carbon fiber; nickel; nickel oxide; interfacial polarization; microwave absorption

1. Introduction

With the rapid development of electromagnetic technology, electromagnetic waves (EMWs) have been widely used in satellite communications, antenna measurement, and sensing, which are convenient for our daily lives and industrial manufacturing. However, high-energy electromagnetic irradiation and unnecessary electromagnetic interference have caused severe electromagnetic pollution, which not only affects the normal operation of electronic equipment but also seriously endangers human health [1–5]. Accordingly, significant efforts have been made to design and prepare strong microwave absorbing materials (MAMs) to tackle the above issues. In general, high-efficiency MAMs are expected to simultaneously satisfy the demands of high absorption ability, wide absorption band, lightweight, and less thickness [6–9].

Depending on the drastic magnetic loss, traditional metal-based materials, such as ferrite and metal powder, have been developed to absorb EMWs [10–12]. Although they possess fascinating microwave absorption (MA) performance in particular frequencies, the high density and poor chemical stability severely restrict their practical utilization as lightweight and high-efficiency absorbers. Nanostructured carbon materials, such as graphene, carbon nanotube, and carbon fiber (CF), have gradually become ideal MAMs due to their superior dielectric properties and ultra-low density [13–16]. Among them, CF possesses a low percolation threshold and excellent dielectric loss due to the one-dimensional (1D) structure and high conductivity, which are sought after in advanced MAMs [17–18]. π electrons can migrate in the whole CF matrix in the form of free electrons and generate induced dipole moments and polarization current under the action of the EM field, thus consuming EMWs. However, pure CF employed as an absorbent has two drawbacks. First, the high electrical conductivity would greatly impair impedance matching, leading to strong reflection rather than absorption. Second, the single dielectric loss is not conducive to broadband absorption [19–20]. In light of these issues, combining CF with a magnetic metal or metal oxide may be an effective solution for improving impedance matching and magnetic loss [21–22]. For example, Chen *et al*. [23] prepared $FeCo/CoFe_2O_4$/CNF composites using the electrospinning method, and the obtained composites displayed an excellent MA performance with an absorption peak of −52.3 dB. Bandaru *et al*. [24] fabricated Fe_3O_4/cotton-derived CF

✉ Corresponding authors: Shikuo Li E-mail: lishikuo@ahu.edu.cn; Fangzhi Huang E-mail: huangfangzhi@163.com; Hui Zhang E-mail: zhhui@ahu.edu.cn

composites, which displayed a minimum reflection loss (RL_{min}) of −56.8 dB. Zhao *et al*. [25] reported Co_3O_4/N-doped carbon/short CF that showed an optimum MA with an RL_{min} value of −29 dB and an efficient absorption bandwidth (EAB) of 5.44 GHz. However, most of the reported magnetic elements on CFs are irregular or agglomerated, which resulted in higher filler loading (usually higher than 20wt%) in the MA performance. This drawback restricts the further applications of lightweight requirements in aerospace and aviation.

Constructing hierarchical nanoarrays on CF may significantly preserve the lightweight feature due to their large surface area and special three-dimensional (3D) micro/nano structure. In this study, hierarchical CF@NiO/Ni composites were successfully prepared through the *in situ* growing of $Ni(OH)_2$ nanosheet arrays on the CF surface and subsequent annealing treatment. The annealing temperature significantly affected the phase structure and morphologies of the NiO/Ni component. Owing to the efficient synergistic effect of NiO/Ni and CF, the obtained composites presented excellent electromagnetic absorption properties even with ultra-low loading (3wt%). Specifically, the as-prepared CF@NiO/Ni-500 achieved the strongest absorption peak of −43.92 dB and the broadest EAB of 5.64 GHz (covering the whole Ku band). Moreover, the simulation results demonstrate that the CF@NiO/Ni absorbing coating can reduce the radar cross-section (RCS), which is important for electromagnetic stealth. The above results suggest that CF@NiO/Ni composites are promising as lightweight and high-efficient absorbents.

2. Experimental

2.1. Pretreatment of CF

CF (Huangyu Electromagnetic Technology Co., Ltd., China) was first soaked in acetone to remove impurities and then immersed in an HNO_3 solution for surface functionalization.

2.2. Preparation of CF@Ni(OH)$_2$

Typically, 1.0 mmol nickel chloride hexahydrate ($NiCl_2\cdot 6H_2O$) and 1.0 mmol hexamethylenetetramine (HMTA) were dissolved in 30 mL deionized water, and then 0.1 g CF was dispersed into the above solution. After sonication for 30 min, the resulting suspension mixture was transferred into a Teflon-lined autoclave and heated at 90°C for 10 h. Finally, light-green products were repeatedly washed with distilled water and dried at 80°C.

2.3. Preparation of CF@NiO/Ni

Hierarchical CF@NiO/Ni composites were prepared through an annealing process. In detail, the as-prepared CF@Ni(OH)$_2$ precursors were calcined under the nitrogen gas flow at the targeted temperatures (300, 400, 500, and 600°C) for 2 h. Based on the composition from the later characterization and the pyrolysis temperature, the as-prepared samples were denoted as CF@NiO-300, CF@NiO/Ni-400, CF@NiO/Ni-500, and CF@Ni-600.

2.4. Characterization

The crystal structure of the samples was identified via X-ray diffraction (XRD, Rigaku Smartlab Beijing Co., LTd., China). The morphologies and nanostructures were investigated via field emission scanning electron microscopy (FE-SEM, Zeiss, Sigma 500, Germany) and transmission electron microscopy (TEM, FEI Tecnai TF20, USA). The element distribution was conducted with an energy-dispersive X-ray spectrometer (EDS, Oxford Ultim Max 40, England) attached to the SEM. The graphitization degree of carbon was measured by a Raman spectrometer (inVia Reflex, England). X-ray photoelectron spectroscopy (ESCALAB 250, USA) was adopted to perform elemental analysis and determine the composition of the material. The composites (3wt%) were mixed with molten paraffin and pressed into toroidal specimens with an outer diameter of 7.00 mm and an inner diameter of 3.04 mm, and their electromagnetic parameters were measured using a vector network analyzer (Agilent E8363B, USA) in 2–18 GHz. Monostatic RCS simulations were performed on the commercial Computer Simulation Technology (CST) Studio Suite 2020. A 180 mm × 180 mm × 2 mm perfect electric conductor (PEC) was used as a metal plate to reflect the EMWs.

3. Results and discussion

3.1. Crystal structure and morphology analysis

Fig. 1(a) depicts the preparation procedure of hierarchical CF@NiO/Ni composites. First, the hierarchical CF@Ni(OH)$_2$ precursors are fabricated through a hydrothermal method. During the hydrothermal process, the HMTA is decomposed to generate an alkaline environment. Then, Ni^{2+} and OH^- in the solution system combine to form layered metal hydroxides (Fig. S1(a)), which are vertically anchored on the CF's surface. Second, the obtained CF@Ni(OH)$_2$ precursors are directly annealed under an N_2 atmosphere. The $Ni(OH)_2$ can be converted into NiO or metallic Ni depending on the annealing temperature. Meanwhile, nanosheets form porous structures due to high temperature dehydration decomposition. The XRD patterns (Fig. 1(b)) show a broad peak at around 25.5°, which corresponds to the (002) plane of the CF substrate [26]. There are three typical characteristic peaks at the 2θ values of 37.26°, 43.28°, and 62.72° (denoted with ♣) in CF@NiO-300 correspond to the (101), (012), and (110) planes of NiO (JCPDS No. 44-1159). When the annealing temperature is 400°C, besides the NiO diffraction peaks, two discernable small diffraction peaks appear at around 44.50° and 51.85° (denoted with ♦), which correspond to the (111) and (200) crystal planes of Ni, respectively (JCPDS No. 04-0850). The phase transition of NiO into Ni is demonstrated due to the reduction of carbon at high temperatures. For CF@NiO/Ni-500, the intensity of the Ni diffraction peak is reinforced, implying that more Ni is produced in the composite. Finally, when extending the annealing temperature to

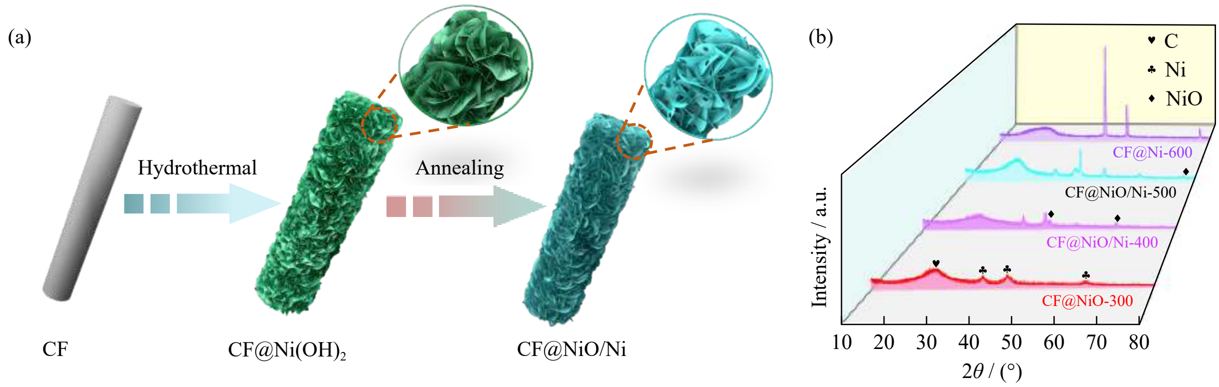

Fig. 1. (a) Schematic preparation procedure of CF@NiO/Ni composites; (b) XRD patterns of CF@NiO/Ni composites obtained at different annealing temperatures.

600°C, the diffraction peaks belong to NiO disappeared, and only Ni diffraction peaks can be observed, demonstrating the total conversion. The XRD results indicate that the phase structure of the CF@NiO/Ni composites can be modulated by adjusting the annealing temperature.

Fig. 2 presents the morphologies of the hierarchical CF@NiO/Ni composites. As shown in Fig. 2(a), the CF@NiO-300 displays uniform leaf-like morphology, and the vertical NiO nanosheets have a flat and smooth surface which is similar to $Ni(OH)_2$ precursors (Fig. S1(b)). Moreover, these nanosheets are cross-linked, forming a stable 3D microporous structure, which allows incident microwaves to be reflected multiple times and thus consumed. At annealing temperatures of 400 and 500°C, the sheet-like morphology of NiO/Ni can still be preserved but become loose and porous (Fig. 2(b) and (c)). As shown in Fig. 2(c), the edges of the sheets of CF@NiO/Ni-500 become slightly

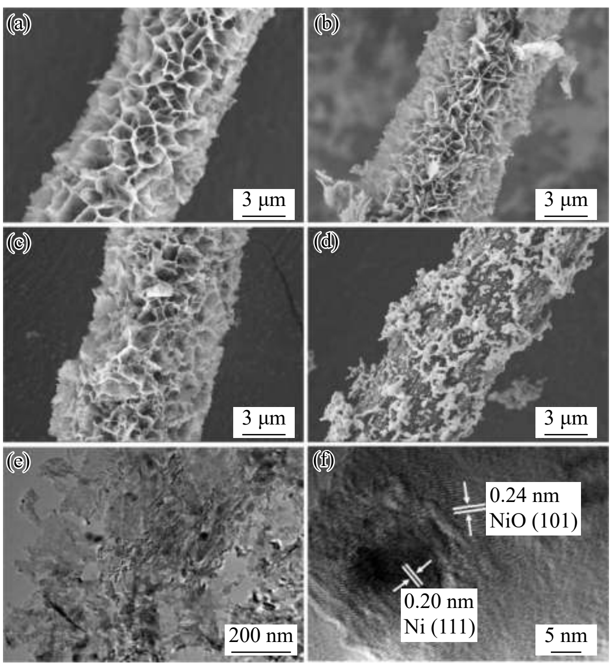

Fig. 2. SEM images of CF@NiO/Ni composites: (a) CF@NiO-300, (b) CF@NiO/Ni-400, (c) CF@NiO/Ni-500, and (d) CF@Ni-600; (e) TEM image and (f) HR-TEM image of CF@NiO/Ni-500.

curly, resulting from the conversion of NiO during the annealing process. However, when the temperature continued to increase, the small Ni nanocrystals agglomerated and formed irregular nanoparticles, leading to the destruction of the nanosheet for CF@Ni-600 (Fig. 2(d)). The TEM image also shows the porous structure of the NiO/Ni, and the discrete Ni nanoparticles are deposited on the porous NiO flakes (Fig. 2(e)). In addition, the high-resolution (HR-TEM image (Fig. 2(f)) exhibits two types of lattice fringes with interlayer distances of 0.24 and 0.20 nm, referring to the (101) crystal plane of NiO and the (111) crystal plane of metal Ni, respectively [27]. The HR-TEM results confirm the multi-heterojunction interface between NiO and Ni, which is in accordance with the former XRD results and the morphology revolution corresponding to the phase modulation. The element mapping in Fig. S2 indicates the coexistence and homogeneous distribution of the Ni and O elements on the CF surface.

3.2. Surface structure and chemical state analysis

Furthermore, Raman spectroscopy was used to illustrate the graphitization degree of C in the CF and CF@NiO/Ni-500 composite. In Fig. 3(a), two broad peaks at ~1340 and 1580 cm^{-1} arise from the disordered carbon (D band) and graphitic structure (G band). In particular, the CF@NiO/Ni-500 has a prominent peak at ~485 cm^{-1}, which is assigned to the first-order longitudinal optical (1LO) mode of Ni–O [28–29]. The intensity ratios of D band and G band (I_D/I_G) are 0.8 and 0.93 for CF and CF@NiO/Ni-500, respectively. This finding reveals that the original sp^2 hybridization system on the annealed CF surface is disrupted to produce more defect sites. These can act as polarization centers to provoke dipole polarization and thus consume electromagnetic energy [30].

The survey XPS spectrum in Fig. 3(b) proves the presence of the Ni, C, and O elements in CF@NiO/Ni-500, which is consistent with the EDS results. The electron interaction between the heterostructures was investigated by analyzing high-resolution Ni 2p spectra. For CF@NiO-300, the detailed Ni 2p spectrum is deconvoluted into two characteristic peaks at 855.5 and 872.6 eV, which are ascribed to Ni $2p_{3/2}$ and Ni $2p_{1/2}$, respectively. The peaks located at 860.9 and 879.3 eV (denoted as “Sat.”) are the satellites of the Ni $2p_{3/2}$

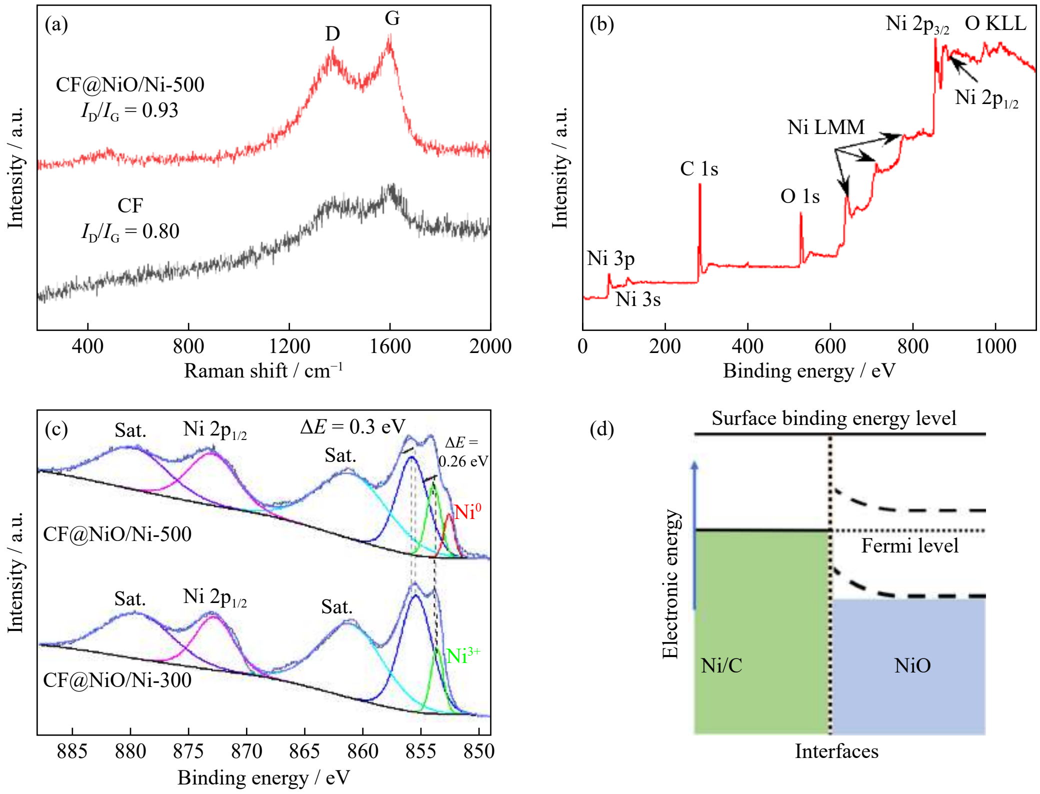

Fig. 3. (a) Raman spectra of CF and CF@NiO/Ni-500; (b) XPS survey spectrum of CF@NiO/Ni-500; (c) XPS Ni 2p spectra of CF@NiO-300 and CF@NiO/Ni-500; (d) illustration of the electron transfer in the integrated NiO and Ni/C.

and Ni 2p$_{1/2}$, respectively [31–32]. In particular, there is no Ni^0 peak in the CF@NiO-300, confirming the absence of Ni metal, which is in accordance with the XRD result. Meanwhile, Ni 2p in CF@NiO/Ni-500 shows a new split peak at approximately 852.7 eV, corresponding to the metallic Ni characteristics, demonstrating the coexistence of metallic and oxidized states. Compared with CF@NiO-300 (853.4 and 855.5 eV for Ni), the binding energy of Ni^{2+} in CF@NiO/Ni-500 appears slightly positive shifts (ca. 0.3 eV for Ni^{2+} and 0.26 eV for Ni^{3+}), indicating the intense electronic interaction and more charge aggregation/redistribution at the NiO–Ni contact interface (Fig. 3(c)). Differences in work functions have been reported in interfacial charges' redistribution and accumulation, resulting in interfacial polarization [33–34]. In general, the work function of metals is higher than that of the corresponding oxide semiconductors. In the NiO/Ni system, the NiO semiconductor energy band is bent to form a Schottky barrier at the heterogeneous interface [35]. The Schottky barrier causes a high interfacial contact resistance, which hinders electron hopping and enriches positive and negative charges at the opposite parties of the interface (Fig. 3(d)). When subjected to periodic electromagnetic fields, positive and negative charges dissipate electromagnetic energy through a strong polarization behavior. Due to the high electron mobility of CF, a similar polarization phenomenon occurs at the Ni–C interface.

3.3. Electromagnetic parameter analysis

To verify the potential feasibility of the system in improving the MA performance, the frequency-dependent electromagnetic parameters (including real parts (ε') and imaginary parts (ε'') of the complex permittivity and real parts (μ') and imaginary parts (μ'') of the relative complex permeability) of CF and CF@NiO/Ni composites were measured. Due to the high electrical conductivity and high aspect ratio of CF, a conductive network can be formed even at low filler loadings [36]. As observed in Fig. S3, the ε'' values of the pure CF are too high, which is detrimental to the microwave attenuation owing to the poor impedance matching [37–38]. Nonetheless, after coating the porous NiO/Ni nanosheet arrays, the ε' and ε'' of the composites decrease (Fig. 4(a) and (b)). This phenomenon can be interpreted with the high resistivity of NiO/Ni nanosheet arrays adequately preventing the conductive network's formation and reducing the CF's space charge polarization [39]. Furthermore, the ε' value dramatically increases from 4.6 (CF@NiO-300) to 10.3 (CF@NiO/Ni-400), 12.4 (CF@NiO/Ni-500), and 16.6 (CF@ Ni-600) at 2.0 GHz, while the ε'' dramatically increases from 0.08 (CF@NiO-300) to 6.0 (CF@NiO/Ni-400), 7.7 (CF@NiO/Ni-400) and 13.8 (CF@Ni-400) at 2.0 GHz, suggesting that the increment metallic Ni content can strengthen the dielectric properties. The ε' curve of CF@NiO/Ni-500 exhibits a fluctuation at approximately 9 GHz, which is probably related to the interfacial polarization caused by the NiO–Ni contact interface and porous structure [40]. To further explain the dielectric behavior of CF@NiO/Ni composites, the Debye model is analyzed based on the measured relative complex permittivity. Under the action of the periodic electric field, the electric dipole will move along with the changes in the electric field. When the electric field frequency increases to a certain degree, the change in the dipole will gradually fail to keep up with the change in the periodic

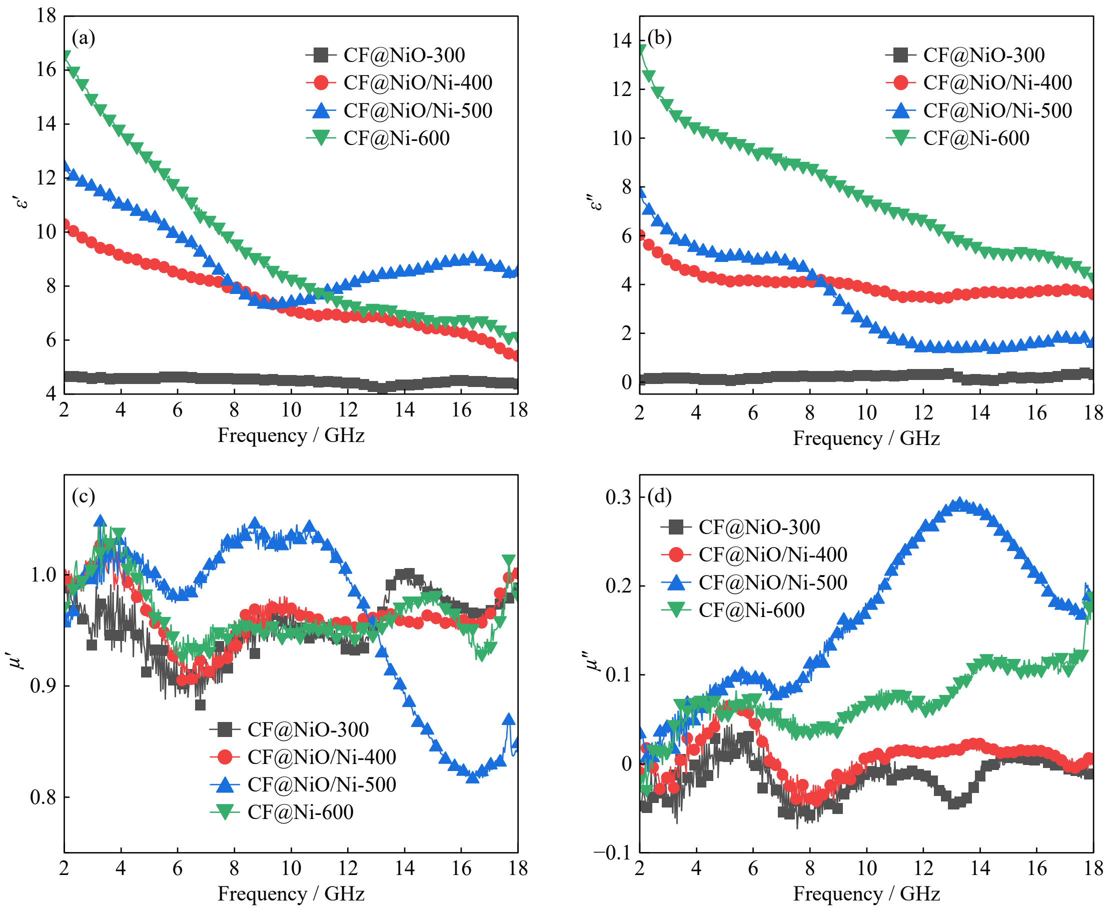

Fig. 4. (a) Real and (b) imaginary parts of complex permittivity and (c) real and (d) imaginary parts of complex permeability of CF@NiO/Ni composites.

frequency of the electric field, thus causing the hysteresis phenomenon and finally reaching the limit. This process can cause the dissipation of electromagnetic energy at high frequencies and even ultra-high frequencies. Thus far, the Debye equation is recognized as a practical theory for understanding polarization loss processes [41]:

$$\left(\varepsilon' - \frac{\varepsilon_s + \varepsilon_\infty}{2}\right)^2 + (\varepsilon'')^2 = \left(\frac{\varepsilon_s - \varepsilon_\infty}{2}\right)^2 \quad (1)$$

where ε_s represents the permittivity at the electrostatic field and ε_∞ represents the permittivity at the high-frequency limit.

According to Eq. (1), the semicircle in the ε' versus ε'' curve is usually called the Cole–Cole semicircle showing a Debye relaxation process. The CF@NiO/Ni-400 and CF@NiO/Ni-500 composites have three semicircles (Fig. S4), which are numerically superior to those in CF@NiO-300 (one) and CF@Ni-600 (two), implying that the former has more polarization relaxation processes. The increased polarization behavior may originate from two aspects: First, the NiO/Ni nanosheet arrays immobilized on the CF surface provide abundant Ni-C contact sites. Second, the NiO-to-Ni conversion creates several Schottky contact interfaces.

The μ' values of the samples fluctuate between 0.81 and 1.05, and the μ'' values vary between –0.07 and 0.3 (Fig. 4(c) and (d)). Moreover, there are several apparent fluctuations appearing at some special frequencies, which are likely to be related to the ferromagnetic resonance and eddy current effect. If the eddy current loss is the primary source of the magnetic loss, the eddy current loss C_0 ($C_0 = \mu''(\mu')^{-2} f^{-1}$, herein f represents the frequency) value should keep stable as the frequency varies. Fig. S5 reveals that the C_0 curves of all samples have several apparent fluctuations, demonstrating that natural and exchange resonances jointly contribute to the magnetic loss of the CF@NiO/Ni composites. Moreover, CF@NiO-300 and CF@NiO/Ni-400 have negative values of μ'' at low frequency range. This phenomenon is possibly attributed to the radiation of the magnetic field energy from the composites.

3.4. MA performance analysis

Quantitative parameters such as RL can be used to assess MA performance. The RL of the CF@NiO/Ni composites is calculated as follows [42–44]:

$$\mathrm{RL} = 20 \cdot \lg \left| \frac{Z_{in} - Z_0}{Z_{in} + Z_0} \right| \quad (2)$$

$$Z_{in} = Z_0 \sqrt{\mu_r/\varepsilon_r} \tanh\left[\mathrm{j}(2\pi f d/c)\sqrt{\mu_r \varepsilon_r}\right] \quad (3)$$

where Z_0 and Z_{in} are the impedance of air and the absorber, and f, d, and c represent the frequency of EMWs, thickness, and velocity of light, respectively. ε_r and μ_r are the complex permittivity ($\varepsilon_r = \varepsilon' - \mathrm{j}\varepsilon''$) and complex permeability ($\mu_r = \mu' - \mathrm{j}\mu''$), respectively.

Fig. 5(a)–(h) shows the MA performance of specimens containing 3wt% composites with various thicknesses. For pure CF, the RL_{min} value is only −5.74 dB (Fig. S6), and such a weak MA property is attributed to its poor impedance matching. As displayed in Fig. 5(a) and (e), the CF@NiO-300 merely holds a negligible absorption performance, which can be explained by the insufficient low permittivity to effectively dissipate EMWs. After adequately adjusting their phase structure, the composites significantly exhibit an enhanced MA. For CF@NiO/Ni-400, the optimal absorption peak of −25.85 dB is significantly more potent than those of CF and CF@NiO-300, and its EAB can reach 6.40 GHz with a matching thickness of 2.25 mm. When the temperature increases to 500°C, the CF@NiO/Ni-500 composite exhibits a powerful electromagnetic absorption. It has an optimal absorption peak value of about −43.92 dB at 17.72 GHz. When the matching thickness is 1.80 mm, its broadest EAB is 5.64 GHz from 12.36 to 18 GHz, covering the whole Ku band. These outstanding achievements make the CF@NiO/Ni-500 composite a promising candidate for EM absorption. However, as the annealing temperature further rises, the absorption intensity and EAB decrease. As shown in Fig. 5(d) and (h), CF@Ni-600 shows inferior performance to CF@NiO/Ni-500, and its RL_{min} value is only −11.78 dB, and the EAB is 4.08 GHz. Together, the composites' phase transitions and unique porous structures likely regulate their diverse MA performance. To clearly and intuitively display the MA performance of the samples, the property parameters are listed in Table 1. These data demonstrate that successfully modulating the phase structure and optimizing the porous structure have great potential in preparing advanced carbonaceous absorbing materials.

3.5. MA mechanism analysis

Generally, poor impedance matching causes intense reflection at the front surface, whereas low attenuation capability results in weak loss capacity. Therefore, proper impedance matching characteristics and strong EMW attenuation are prerequisites for developing an ideal absorber. Thus, the normalized impedance matching ratio ($Z_r = |Z_{in}/Z_0|$) and the attenuation coefficient (α) of the CF@NiO/Ni composites are calculated to provide a basis for the further elucidation of the enhanced MA performance [45–46].

$$Z_r = \left|\frac{Z_{in}}{Z_0}\right| = \left|\sqrt{\mu_r/\varepsilon_r}\tanh\left[j(2\pi f d/c)\sqrt{\mu_r\varepsilon_r}\right]\right| \tag{4}$$

$$\alpha = \frac{\sqrt{2}\pi f}{c}\times \sqrt{(\mu''\varepsilon''-\mu'\varepsilon')+\sqrt{(\mu''\varepsilon''-\mu'\varepsilon')^2+(\mu''\varepsilon'+\mu'\varepsilon'')^2}} \tag{5}$$

The Z_r and α curves of all the samples are shown in Fig. 6 (a) and (b). From Fig. 6(a), CF@NiO/Ni-500 exhibits a satisfactory impedance matching characteristic, implying that most incident EMWs penetrate the inside of the CF@NiO/Ni-500 matrix and thereby are attenuated. Although CF@Ni-600 possesses the highest α (Fig. 6(b)), the unsatisfactory Z_r produced a poor MA performance. Therefore, the enhanced MA capabilities of the CF@NiO/Ni-500 composite can be attributed to the high attenuation coefficient and good impedance matching.

In addition, electromagnetic energy can be consumed by the "geometric effect." This special loss is called quarter-

Table 1. MA properties of CF and CF@NiO/Ni

Sample	RL / dB	Frequency / GHz	Thickness / mm	EAB / GHz
CF	−5.74	18.00	1.50	0
CF@NiO-300	−2.41	17.72	2.60	0
CF@NiO/Ni-400	−25.85	7.44	2.25	6.40
CF@NiO/Ni-500	−43.92	17.72	1.80	5.64
CF@Ni-600	−11.78	17.68	1.80	4.08

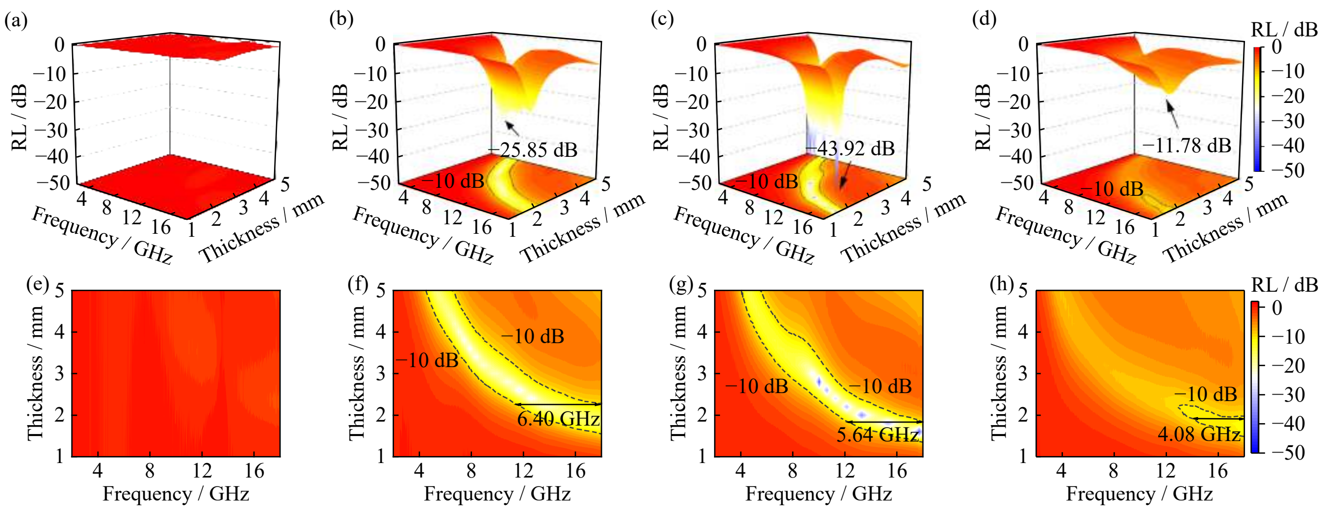

Fig. 5. Frequency dependences of 3D and 2D RL maps of (a, e) CF@NiO-300, (b, f) CF@NiO/Ni-400, (c, g) CF@NiO/Ni-500, and (d, h) CF@Ni-600.

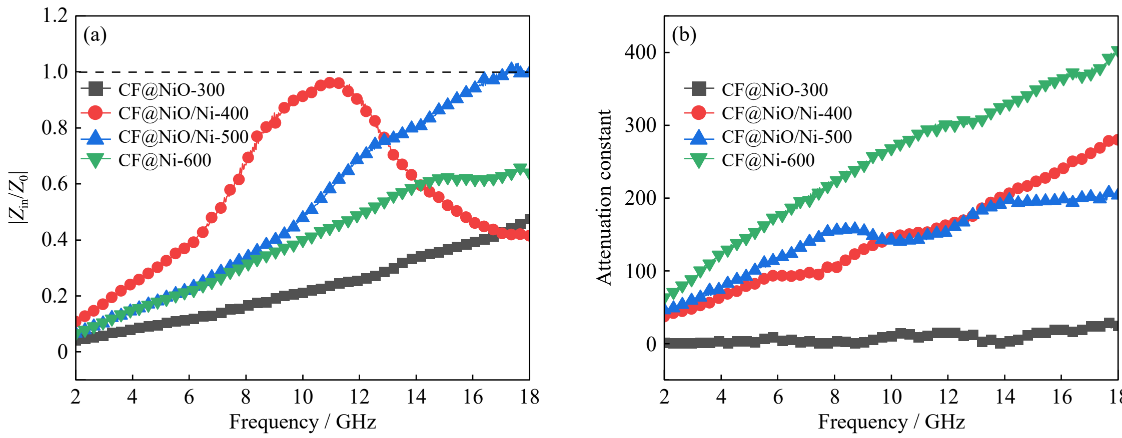

Fig. 6. (a) Impedance matching ratio and (b) attenuation coefficient for the CF@NiO/Ni composites.

wavelength cancellation ($n\lambda/4$), which can be described as

$$t_{\mathrm{m}} = \frac{n\lambda}{4} = \frac{nc}{4f_{\mathrm{m}}\sqrt{|\varepsilon_{\mathrm{r}}||\mu_{\mathrm{r}}|}}\ (n = 1,3,5,\ldots) \tag{6}$$

where t_m and f_m are the thickness and frequency corresponding to the RL_{min} peaks, λ is the wave-length of microwave, $|\varepsilon_r|$ and $|\mu_r|$ are the modulus of ε_r and μ_r, and n represents the positive odd number [47–48]. Fig. S7 shows the RL and t_m versus f_m curves of the CF@NiO/Ni-500 composites. All the experimental thicknesses (red pentacle) are precisely located on the simulated t_m curves (green line), which demonstrates that the quarter-wavelength cancellation theory has an important reference for analyzing the enhancement of the CF@NiO/Ni-500 MA performance properties.

The structural model of the CF@NiO/Ni composites and the possible MA mechanism are shown in Fig. 7(a). The enhancement of the MA performance can be summarized as follows: (1) The metal oxide array coating and its phase structure transformation optimize the impedance matching characteristics. This result is ascribed to the high resistivity of NiO/Ni nanosheet arrays, which appropriately prevent the establishment of a conductive network and reduce the space-charge polarization of CF. (2) Several heterogeneous interfaces are generated during the phase transition process, and the induced charge accumulation and redistribution at these

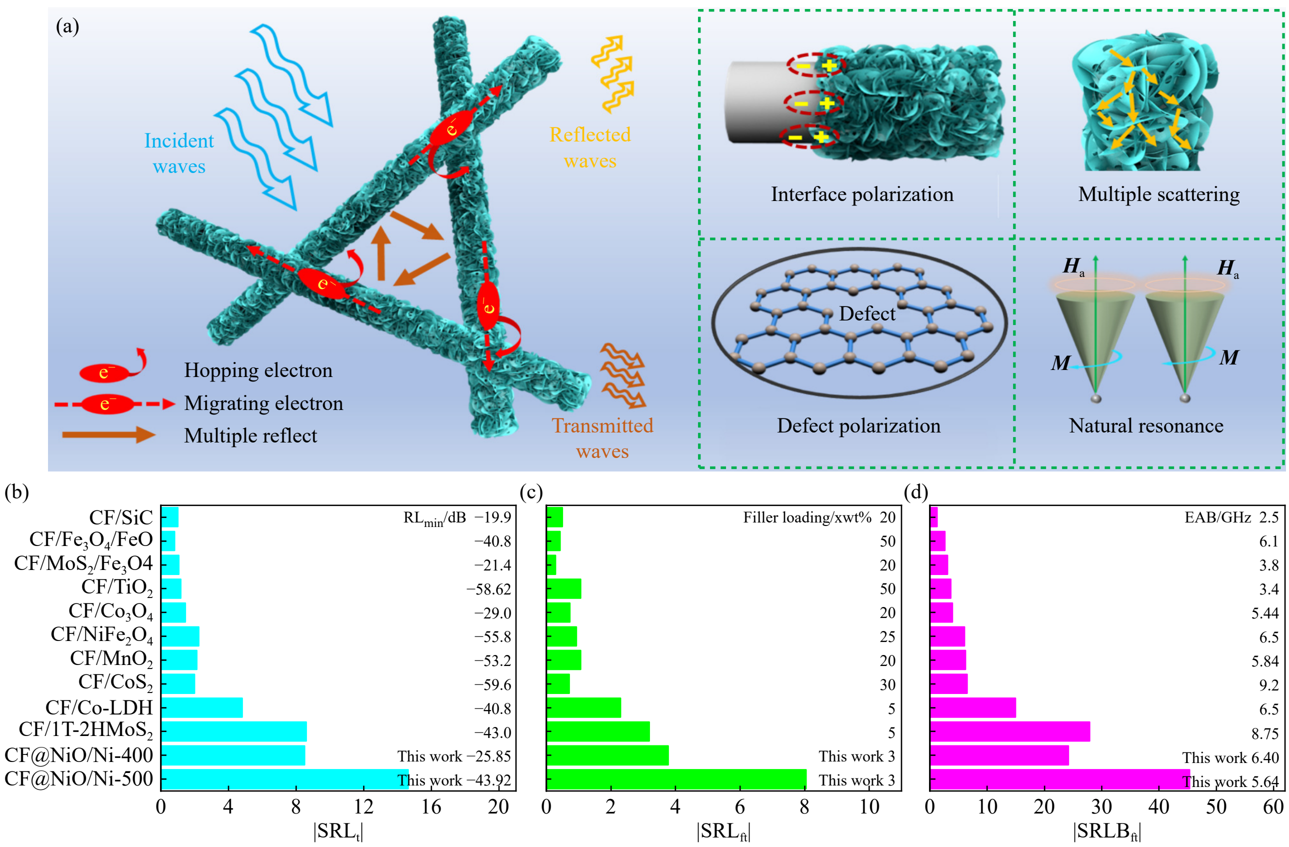

Fig. 7. (a) Schematic illustration of the MA mechanisms in CF@NiO/Ni composites; comparison of (b) $|SRL_t|$, (c) $|SRL_{ft}|$, and (d) $|SRLB_{ft}|$ of CF@NiO/Ni composites with those of other CF-based MAMs. *M*—Induced electromagnetic field; H_a—Applied magnetic field.

interfaces promote the interfacial polarization loss. (3) The effective cooperation of dielectric and magnetic losses endows CF@NiO/Ni composites with an excellent MA behavior. (4) The unique 3D porous configuration of NiO/Ni arrays can provide multiple reflecting and scattering abilities, resulting in more incident EMWs being consumed.

Recently, a series of objective and precise criteria, including specific reflection loss SRL_t (RL/layer thickness), SRL_{ft} (RL/(filler loading × layer thickness)), and $SRLB_{ft}$ (RL × EAB/(filler loading × layer thickness)), have been proposed to further comprehensively evaluate the MA performance of MAMs [49–51]. Based on these methods, the $|SRL_t|$, $|SRL_{ft}|$, and $|SRLB_{ft}|$ of CF@NiO/Ni composites and other representative CF-based MAMs are calculated, and the results are shown in Fig. 7(b)–(d). It can be seen that the CF@NiO/Ni-500 exhibits superior performance to its counterparts, implying its great prospect as a high-efficiency MAM. The detailed MA parameters are listed in Table S1.

3.6. RCS simulation

In practical applications, EMWs are obliquely incident on the coating at certain angles. Therefore, in aircraft stealth design, EMWs at different angles of incidence need to be counteracted [52]. A CST program is used to simulate RCS with characteristic sample coatings and incidence angles from −90° to 90° (Fig. 8(a)). As shown in Fig. 8(b), the RCS values of the PEC and CF are high, indicating their strong reflection and low absorption characteristic. By contrast, the RCS values are significantly reducing after coating CF@NiO/Ni, indicating that the porous hierarchical CF@NiO/Ni structure positively impacts MA. Similarly, in Fig. S8(a)–(d), the model coated with CF@NiO/Ni-400 has the strongest RCS reduction in all directions, which is attributed to its broad absorption bandwidth.

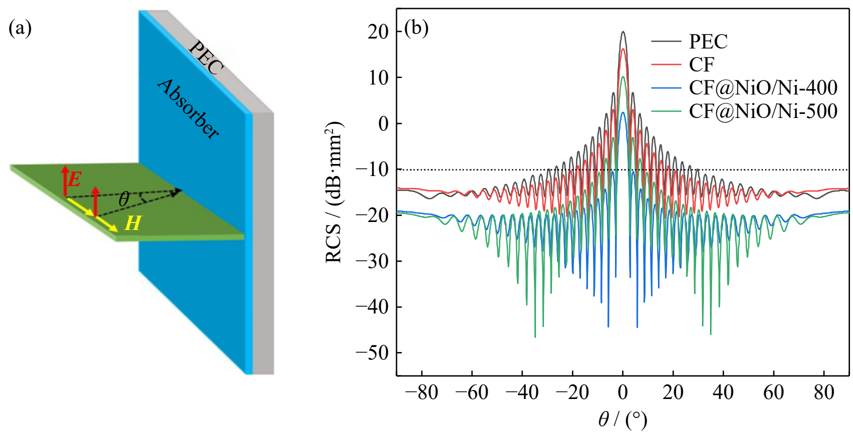

Fig. 8. (a) Schematic illustration of the simulated cubic model (*E*—Electric field; *H*—Magnetic field; *θ*—Angle of incidence of EMWs); (b) RCS values of PEC, CF, CF@NiO/Ni-400, and CF@NiO/Ni-500.

4. Conclusion

In summary, porous NiO/Ni nanosheet arrays are successfully constructed on the CF surface using the hydrothermal method and subsequent annealing treatment. The phase and morphology of the coating can be tuned by adjusting the annealing temperature, which significantly affects the complex permittivity and impedance matching of hierarchical CF@NiO/Ni composites. The tailored composition and hierarchical structure synergistic effect endow the CF@NiO/Ni-500 with a superior MA performance. In particular, the CF@NiO/Ni-500 achieves an RL_{min} value of −43.92 dB and a broad EAB of 5.64 GHz (covering the whole Ku band) at an ultra-low loading of 3wt%. The simulated RCS results reveal that the strong electromagnetic scattering can be effectively suppressed by employing CF@NiO/Ni composites on the PEC. We hope that this work could inspire the design of novel CF-based composites for MA via phase and morphology evolution.

Acknowledgements

This work was financially supported by the National Natural Science Foundation of China (Nos. 51872002 and 52172174), and the key research and development projects in Anhui province, China (No. 202004a07020026). We also gratefully acknowledge the support of Joint Laboratory of Electromagnetic Material Structure Design and Advanced Stealth Technology.

Conflict of Interest

The authors declare no competing financial interest.

Supplementary Information

The online version contains supplementary material available at https://doi.org/10.1007/s12613-022-2524-2.

References

[1] B.Y. Taishi, Y.T. Yang, X.Q. Wu, J.C. Xu, and S.G. Huang, Dual-band 3D electrically small antenna based on split ring resonators, *Adv. Compos. Hybrid Mater.*, 5(2022), No. 1, p. 350.

[2] Y. Zhang, Y. Huang, T.F. Zhang, *et al.*, Broadband and tunable high-performance microwave absorption of an ultralight and

highly compressible graphene foam, *Adv. Mater.*, 27(2015), No. 12, p. 2049.
[3] X.L. Li, X.W. Yin, C.Q. Song, *et al.*, Self-assembly core-shell graphene-bridged hollow MXenes spheres 3D foam with ultrahigh specific EM absorption performance, *Adv. Funct. Mater.*, 28(2018), No. 41, art. No. 1803938.
[4] Q.H. Liu, Q. Cao, H. Bi, *et al.*, CoNi@SiO_2@TiO_2 and CoNi@Air@TiO_2 microspheres with strong wideband microwave absorption, *Adv. Mater.*, 28(2016), No. 3, p. 486.
[5] S. ur Rehman, J.M. Wang, Q.H. Luo, *et al.*, Starfish-like C/$CoNiO_2$ heterostructure derived from ZIF-67 with tunable microwave absorption properties, *Chem. Eng. J.*, 373(2019), p. 122.
[6] X.L. Li, X.W. Yin, H.L. Xu, *et al.*, Ultralight MXene-coated, interconnected SiCnws three-dimensional lamellar foams for efficient microwave absorption in the X-band, *ACS Appl. Mater. Interfaces*, 10(2018), No. 40, p. 34524.
[7] L.Y. Liang, R.S. Yang, G.J. Han, *et al.*, Enhanced electromagnetic wave-absorbing performance of magnetic nanoparticles-anchored 2D $Ti_3C_2T_x$ MXene, *ACS Appl. Mater. Interfaces*, 12(2020), No. 2, p. 2644.
[8] L.S. Xing, X. Li, Z.C. Wu, *et al.*, 3D hierarchical local heterojunction of MoS_2/FeS_2 for enhanced microwave absorption, *Chem. Eng. J.*, 379(2020), art. No. 122241.
[9] M. Green and X.B. Chen, Recent progress of nanomaterials for microwave absorption, *J. Materiomics*, 5(2019), No. 4, p. 503.
[10] J.L. Liu, H.S. Liang, Y. Zhang, G.L. Wu, and H.J. Wu, Facile synthesis of ellipsoid-like $MgCo_2O_4/Co_3O_4$ composites for strong wideband microwave absorption application, *Composites Part B*, 176(2019), art. No. 107240.
[11] W.J. Duan, X.D. Li, Y. Wang, *et al.*, Surface functionalization of carbonyl iron with aluminum phosphate coating toward enhanced anti-oxidative ability and microwave absorption properties, *Appl. Surf. Sci.*, 427(2018), p. 594.
[12] P. Zhou, J.H. Chen, M. Liu, P. Jiang, B. Li, and X.M. Hou, Microwave absorption properties of SiC@SiO_2@Fe_3O_4 hybrids in the 2–18 GHz range, *Int. J. Miner. Metall. Mater.*, 24(2017), No. 7, p. 804.
[13] P.B. Liu, Y.Q. Zhang, J. Yan, Y. Huang, L. Xia, and Z.X. Guang, Synthesis of lightweight N-doped graphene foams with open reticular structure for high-efficiency electromagnetic wave absorption, *Chem. Eng. J.*, 368(2019), p. 285.
[14] X.Y. Zhu, H.F. Qiu, P. Chen, G.Z. Chen, and W.X. Min, Anemone-shaped ZIF-67@CNTs as effective electromagnetic absorbent covered the whole X-band, *Carbon*, 173(2021), p. 1.
[15] G.Z. Shen, B.Q. Mei, H.Y. Wu, H.Y. Wei, X.M. Fang, and Y.W. Xu, Microwave electromagnetic and absorption properties of N-doped ordered mesoporous carbon decorated with ferrite nanoparticles, *J. Phys. Chem. C*, 121(2017), No. 7, p. 3846.
[16] J.Q. Wang, L. Liu, S.L. Jiao, K.J. Ma, J. Lv, and J.J. Yang, Hierarchical carbon Fiber@MXene@MoS_2 core-sheath synergistic microstructure for tunable and efficient microwave absorption, *Adv. Funct. Mater.*, 30(2020), No. 45, art. No. 2002595.
[17] Y.S. Wei, J.L. Yue, X.Z. Tang, Z.J. Du, and X.Z. Huang, Enhanced magnetic and microwave absorption properties of FeCo-SiO_2 nanogranular film functionalized carbon fibers fabricated with the radio frequency magnetron method, *Appl. Surf. Sci.*, 428(2018), p. 296.
[18] D.D. Min, W.C. Zhou, Y.C. Qing, F. Luo, and D.M. Zhu, Highly oriented flake carbonyl iron/carbon fiber composite as thin-thickness and wide-bandwidth microwave absorber, *J. Alloys Compd.*, 744(2018), p. 629.
[19] P.B. Liu, C.Y. Zhu, S. Gao, C. Guan, Y. Huang, and W.J. He, N-doped porous carbon nanoplates embedded with CoS_2 vertically anchored on carbon cloths for flexible and ultrahigh microwave absorption, *Carbon*, 163(2020), p. 348.
[20] Z. Cheng, Y.S. Cao, R.F. Wang, *et al.*, Hierarchical surface engineering of carbon fiber for enhanced composites interfacial properties and microwave absorption performance, *Carbon*, 185(2021), p. 669.
[21] Y.S. Huo, Y.J. Tan, K. Zhao, Z.X. Lu, L.Y. Zhong, and Y.F. Tang, Enhanced electromagnetic wave absorption properties of Ni magnetic coating-functionalized SiC/C nanofibers synthesized by electrospinning and magnetron sputtering technology, *Chem. Phys. Lett.*, 763(2021), art. No. 138230.
[22] H.S. Liang, H. Xing, M. Qin, and H.J. Wu, Bamboo-like short carbon fibers@Fe_3O_4@phenolic resin and honeycomb-like short carbon fibers@Fe_3O_4@FeO composites as high-performance electromagnetic wave absorbing materials, *Composites Part A*, 135(2020), art. No. 105959.
[23] J.B. Chen, J. Zheng, Q.Q. Huang, F. Wang, and G.B. Ji, Enhanced microwave absorbing ability of carbon fibers with embedded FeCo/$CoFe_2O_4$ nanoparticles, *ACS Appl. Mater. Interfaces*, 13(2021), No. 30, p. 36182.
[24] S. Bandaru, N. Murthy, R. Kulkarni, and N.J. English, Magnetic ferrite/carbonized cotton fiber composites for improving electromagnetic absorption properties at gigahertz frequencies, *J. Mater. Sci. Technol.*, 86(2021), p. 127.
[25] Z.H. Zhao, K.C. Kou, and H.J. Wu, 2-Methylimidazole-mediated hierarchical Co_3O_4/N-doped carbon/short-carbon-fiber composite as high-performance electromagnetic wave absorber, *J. Colloid Interface Sci.*, 574(2020), p. 1.
[26] C. Chen, J.B. Xi, E.Z. Zhou, L. Peng, Z.C. Chen, and C. Gao, Porous graphene microflowers for high-performance microwave absorption, *Nano-Micro Lett.*, 10(2017), No. 2, p. 1.
[27] L.N. Huang, C.G. Chen, X.Y. Huang, S.C. Ruan, and Y.J. Zeng, Enhanced electromagnetic absorbing performance of MOF-derived Ni/NiO/Cu@C composites, *Composites Part B*, 164(2019), p. 583.
[28] K.N. Patel, M.P. Deshpande, K. Chauhan, *et al.*, Effect of Mn doping concentration on structural, vibrational and magnetic properties of NiO nanoparticles, *Adv. Powder Technol.*, 29(2018), No. 10, p. 2394.
[29] B. Saravanakumar, R. Shobana, G. Ravi, V. Ganesh, and R. Yuvakkumar, Pseudocapacitive NiO/$NiSnO_3$ electrode for supercapacitor applications, *J. Electron. Mater.*, 47(2018), No. 11, p. 6390.
[30] S.P. Wang, Q.S. Li, K. Hu, S.N. Wang, Q.C. Liu, and X.K. Kong, A facile synthesis of bare biomass derived holey carbon absorbent for microwave absorption, *Appl. Surf. Sci.*, 544(2021), art. No. 148891.
[31] S.C. Wang, H.L. Liu, J. Hu, *et al., In situ* synthesis of NiO@Ni micro/nanostructures as supercapacitor electrodes based on femtosecond laser adjusted electrochemical anodization, *Appl. Surf. Sci.*, 541(2021), art. No. 148216.
[32] V. Senthilkumar, F.B. Kadumudi, N.T. Ho, *et al.*, NiO nanoarrays of a few atoms thickness on 3D nickel network for enhanced pseudocapacitive electrode applications, *J. Power Sources*, 303(2016), p. 363.
[33] L. Wang, X.F. Yu, X. Li, J. Zhang, M. Wang, and R.C. Che, MOF-derived yolk–shell Ni@C@ZnO Schottky contact structure for enhanced microwave absorption, *Chem. Eng. J.*, 383(2020), art. No. 123099.
[34] J.J. Ding, L. Wang, Y.H. Zhao, *et al.*, Boosted interfacial polarization from multishell TiO_2@Fe_3O_4 @PPy heterojunction for enhanced microwave absorption, *Small*, 15(2019), No. 36, art. No. e1902885.
[35] Y. Yu, C.H. Wang, Y.F. Yu, Y.T. Wang, and B. Zhang, Promoting selective electroreduction of nitrates to ammonia over electron-deficient Co modulated by rectifying Schottky contacts, *Sci. China Chem.*, 63(2020), No. 10, p. 1469.
[36] H. Wu, Y.M. Zhong, Y.X. Tang, *et al.*, Precise regulation of weakly negative permittivity in $CaCu_3Ti_4O_{12}$ metacomposites

by synergistic effects of carbon nanotubes and grapheme, *Adv. Compos. Hybrid Mater.*, 5(2022), No. 1, p. 419.
[37] S.P. Wang, K. Hu, F. Huang, *et al*., Activating microwave absorption via noncovalent interactions at the interface based on metal-free graphene nanosheets, *Carbon*, 152(2019), p. 818.
[38] W. Zhou, L. Long, P. Xiao, *et al*., Silicon carbide nano-fibers *in situ* grown on carbon fibers for enhanced microwave absorption properties, *Ceram. Int.*, 43(2017), No. 7, p. 5628.
[39] Q.C. Liu, Z.F. Zi, M. Zhang, A.B. Pang, J.M. Dai, and Y.P. Sun, Enhanced microwave absorption properties of carbonyl iron/Fe_3O_4 composites synthesized by a simple hydrothermal method, *J. Alloys Compd.*, 561(2013), p. 65.
[40] H.G. Wang, F.B. Meng, F. Huang, *et al*., Interface modulating CNTs@PANi hybrids by controlled unzipping of the walls of CNTs to achieve tunable high-performance microwave absorption, *ACS Appl. Mater. Interfaces*, 11(2019), No. 12, p. 12142.
[41] L. Chai, Y.Q. Wang, Z.R. Jia, *et al*., Tunable defects and interfaces of hierarchical dandelion-like $NiCo_2O_4$ via Ostwald ripening process for high-efficiency electromagnetic wave absorption, *Chem. Eng. J.*, 429(2022), art. No. 132547.
[42] G.B. Sun, B.X. Dong, M.H. Cao, B.Q. Wei, and C.W. Hu, Hierarchical dendrite-like magnetic materials of Fe_3O_4, γ-Fe_2O_3, and Fe with high performance of microwave absorption, *Chem. Mater.*, 23(2011), No. 6, p. 1587.
[43] X. Sun, J.P. He, G.X. Li, *et al*., Laminated magnetic graphene with enhanced electromagnetic wave absorption properties, *J. Mater. Chem. C*, 1(2013), No. 4, p. 765.
[44] F.B. Meng, H.G. Wang, Wei, *et al*., Generation of graphene-based aerogel microspheres for broadband and tunable high-performance microwave absorption by electrospinning-freeze drying process, *Nano Res.*, 11(2018), No. 5, p. 2847.
[45] B.L. Wang, H.Y. Chen, S. Wang, *et al*., Construction of core-shell structured Co_7Fe_3@C nanocapsules with strong wideband microwave absorption at ultra-thin thickness, *Carbon*, 184(2021), p. 223.
[46] Z.H. Wang, L.X. Yang, Y. Zhou, C. Xu, M. Yan, and C. Wu, NiFe LDH/MXene derivatives interconnected with carbon fabric for flexible electromagnetic wave absorption, *ACS Appl. Mater. Interfaces*, 13(2021), No. 14, p. 16713.
[47] N. Yang, Z.X. Luo, G.R. Zhu, *et al*., Ultralight three-dimensional hierarchical cobalt nanocrystals/N-doped CNTs/carbon sponge composites with a hollow skeleton toward superior microwave absorption, *ACS Appl. Mater. Interfaces*, 11(2019), No. 39, p. 35987.
[48] X. Li, L. Wang, W.B. You, *et al*., Morphology-controlled synthesis and excellent microwave absorption performance of $ZnCo_2O_4$ nanostructures via a self-assembly process of flake units, *Nanoscale*, 11(2019), No. 6, p. 2694.
[49] Y.C. Yin, X.F. Liu, X.J. Wei, *et al*., Magnetically aligned co-C/MWCNTs composite derived from MWCNT-interconnected zeolitic imidazolate frameworks for a lightweight and highly efficient electromagnetic wave absorber, *ACS Appl. Mater. Interfaces*, 9(2017), No. 36, p. 30850.
[50] Y. Li, X.F. Liu, X.Y. Nie, *et al*., Multifunctional organic-inorganic hybrid aerogel for self-cleaning, heat-insulating, and highly efficient microwave absorbing material, *Adv. Funct. Mater.*, 29(2019), No. 10, art. No. 1807624.
[51] S.P. Wang, Q.S. Li, K. Hu, Q.C. Liu, X.F. Liu, and X.K. Kong, Activating microwave absorption performance by reduced graphene oxide-borophene heterostructure, *Composites Part A*, 138(2020), art. No. 106033.
[52] J.J. Pan, X. Sun, Z.Z. Jin, *et al*., Constructing two-dimensional lamellar monometallic carbon nanocomposites by sodium chloride hard template for lightweight microwave scattering and absorption, *Composites Part B*, 228(2022), art. No. 109422.